ARTICLES
https://doi.org/10.1038/s41558-021-01212-5

nature climate change

Ocean warming and accelerating Southern Ocean zonal flow

Jia-Rui Shi[1,2]✉, Lynne D. Talley[1], Shang-Ping Xie[1], Qihua Peng[1,3] and Wei Liu[4]

The Southern Ocean (>30° S) has taken up a large amount of anthropogenic heat north of the Subantarctic Front (SAF) of the Antarctic Circumpolar Current (ACC). Poor sampling before the 1990s and decadal variability have heretofore masked the ocean's dynamic response to this warming. Here we use the lengthening satellite altimetry and Argo float records to show robust acceleration of zonally averaged Southern Ocean zonal flow at 48° S–58° S. This acceleration is reproduced in a hierarchy of climate models, including an ocean-eddy-resolving model. Anthropogenic ocean warming is the dominant driver, as large (small) heat gain in the downwelling (upwelling) regime north (south) of the SAF causes zonal acceleration on the northern flank of the ACC and adjacent subtropics due to increased baroclinicity; strengthened wind stress is of secondary importance. In Drake Passage, little warming occurs and the SAF velocity remains largely unchanged. Continued ocean warming could further accelerate Southern Ocean zonal flow.

The Southern Ocean, often defined as the ocean south of about 30° S, has experienced pronounced subsurface warming, widespread surface freshening, increasing anthropogenic carbon and changes in oxygen and chlorofluorocarbons over the past several decades of observations[1–7]. Modelling studies suggest that greenhouse gas increase and stratospheric ozone depletion are major drivers of Southern Ocean change[8–11]. The strength of overturning circulation plays an important role in regulating the exchange of anthropogenic heat at the sea surface and in redistributing oceanic tracers[11–14]. Moreover, horizontal ocean circulation, including the Antarctic Circumpolar Current (ACC) and subtropical gyres, facilitates the exchange of properties across ocean basins[15]. Hence, quantifying how the horizontal circulation changes in the context of global warming is vital to interpreting past climate change and for reliable future climate projections.

Previous studies of changing Southern Ocean circulation have focused mostly on the response to changes in westerly winds, which are shifting poleward and intensifying. These observational and modelling studies, which have largely focused on the ACC in the Drake Passage, have concluded that the Drake Passage transport is insensitive to the increasing wind stress[16–21] and that the additional energy imparted by the wind increase mostly goes into mesoscale eddies[22], an effect known as eddy saturation[23]. Analyses of Argo profiling float and oceanographic data carried out a decade ago showed little change in ACC isopycnal slopes and transport before 2006 even as the winds strengthened[2]. Looking to the north of the ACC, the observed spin-up and ventilation of the subtropical gyres has been hypothesised to coincide with the enhancement of wind-stress forcing[6,7,24,25]. A recent analysis, using data-assimilating models and observations, shows increasing Southern Ocean kinetic energy over recent decades, with speculated attribution to increased wind energy[26].

The relationship between changes in the buoyancy distribution/forcing and Southern Ocean responses has been examined in models[27–29]. It has been shown that surface buoyancy flux change can have an important impact on the subtropical gyres without wind-stress change[30,31]. Buoyancy forcing due to ocean warming has recently been shown to strongly accelerate the zonally averaged Southern Ocean zonal flow in the upper layer (that is, 0–2,000 m), in contrast to much weaker acceleration induced by increased wind stress[14], using the Community Earth System Model (CESM)[32,33]. This is due to the thermal wind response of the zonal flow to greater heat content increase north of the ACC than within it and to the south, which increases the meridional density gradient[14]. This asymmetric warming is due to the background meridional overturning circulation, with deep water upwelling at higher latitudes and northward Ekman transport that redistributes the absorbed heat under global warming[13,34].

What we add here is clear, observational evidence of upper-layer zonal-velocity changes associated with the observed heat-content changes. Argo float observations show remarkable north–south asymmetry in warming over the 0–2,000 m layer in the Southern Ocean during 2006–2013 (ref. [3]). This warming has continued, as shown here, and continues to be much greater in the subtropical region just north of the ACC than within and south of it (Fig. 1). Associated with this warming distribution, we show here a statistically significant acceleration of the Southern Ocean zonal flow between 48° S and 58° S, based on satellite altimeter and Argo float data, independently. We compare the observed buoyancy and velocity changes with historical simulations from the sixth phase of the Coupled Model Intercomparison Project (CMIP6) models and large ensemble simulations and show the connection between external buoyancy forcing and acceleration of Southern Ocean zonal flow. This conclusion is also supported by a CESM eddy-resolving model. Using a hierarchy of idealized general circulation model (GCM) simulations, we find that the magnitude and spatial pattern of the observed zonal flow changes are more likely to arise from buoyancy-forcing change than from wind-stress change.

Observed acceleration of Southern Ocean zonal flow

Zonally averaged sea level has been rising at all latitudes in the Southern Ocean over the 27 years since 1993, based on Archiving

[1]Scripps Institution of Oceanography, University of California San Diego, La Jolla, CA, USA. [2]Woods Hole Oceanographic Institution, Woods Hole, MA, USA. [3]State Key Laboratory of Tropical Oceanography, South China Sea Institute of Oceanology, Chinese Academy of Sciences, Guangzhou, China. [4]Department of Earth and Planetary Sciences, University of California Riverside, Riverside, CA, USA. ✉e-mail: jia-rui.shi@whoi.edu

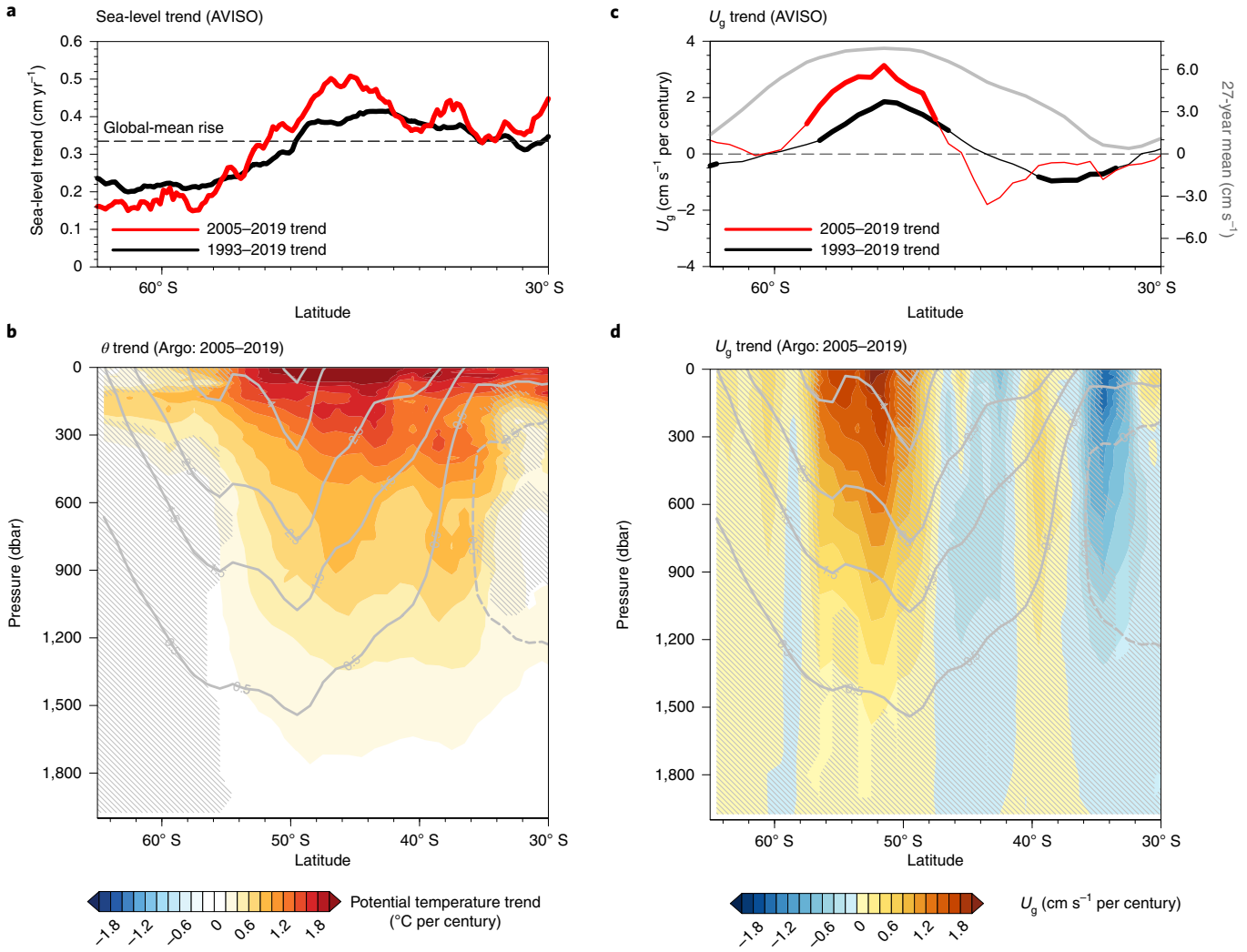

Fig. 1 | Zonal mean sea-level, subsurface temperature and geostrophic velocity trends from observations. a, Zonal mean sea-level trend from AVISO for 1993–2019 (black) and 2005–2019 (red). The global mean sea-level trend (0.33 cm per year from 1993 to 2019) is the dashed black line. **b**, Potential temperature trend (2005–2019) from Argo. **c**, Zonal geostrophic velocity (U_g) trend from AVISO. Climatological (1993–2019) surface U_g (cm s^{-1}) from AVISO is the solid grey curve. **d**, The same from Argo relative to 2,000 dbar. Grey contours in **b** and **d** are the climatological U_g based on Argo (cm s^{-1}), with solid contours representing eastward flow and dashed contours representing westward flow. Hatched regions in **b** and **d** indicate that the trends are not significant at the 95% confidence level from the two-tailed *t* test. Thick curves in **a** and **c** show latitudes exceeding 95% statistical significance.

Validation and Interpretation of Satellite Oceanographic (AVISO) observations (Fig. 1a). Maximum sea-level rise, larger than the global mean, has been at about 45° S, while sea-level increase has been slower within 65° S–50° S. The increasing sea level is attributable to thermal expansion based on gridded Argo temperature data[35] (Fig. 1b). Subsurface zonal-mean warming is maximum at about 45° S on the northern flank of the broad, climatological, zonal-mean eastward flow. On the southern flank, the warming rate is insignificant or much slower, attributed to the upwelling of deep water that has been shown in previous studies[13,14].

Acceleration of the surface eastward geostrophic velocity (U_g) is associated with the increasing sea-level gradient and hence meridional pressure gradient within 45° S–60° S (Fig. 1c). The significant acceleration is concentrated around 48° S–58° S. U_g shows mostly insignificant negative (westward) trends on the north and south sides of the significant positive trend. Thus, the Southern Ocean's eastward flow has intensified and possibly narrowed.

Acceleration of U_g is also apparent from Argo data[35] and decays with depth (Fig. 1d). This baroclinic structure is consistent with buoyancy forcing that creates stronger warming in the upper layer north of the ACC (Fig. 1b), as opposed to wind-forcing changes that have a more barotropic response[14]. For the absolute geostrophic velocity referenced to the U_g based on surface altimetry, we also find acceleration of eastward flow in the upper layer between 48° S and 58° S (Extended Data Fig. 1).

The surface U_g from AVISO altimetry, averaged between 48° S and 58° S, increased for 1993–2019 (Fig. 2). The 27-year linear trend and 95% confidence interval was 0.74 ± 0.25 cm s^{-1} per century. The corresponding trend for 2005–2019 from Argo was a comparable 0.84 ± 0.21 cm s^{-1} per century (Fig. 3c). We also examine datasets from the Institute of Atmospheric Physics (IAP), Met Office Hadley Centre (EN4) and World Ocean Atlas 2018 (WOA18) (Fig. 2a). All three show a significant eastward acceleration of the geostrophic flow relative to 2,000 m since 1993 (Fig. 3c). In addition to the long-term eastward acceleration, the AVISO-based surface U_g shows strong decadal variability as corroborated by EN4 and IAP datasets. In AVISO, the decadal variability obscured the U_g trend through 2010. The eastward

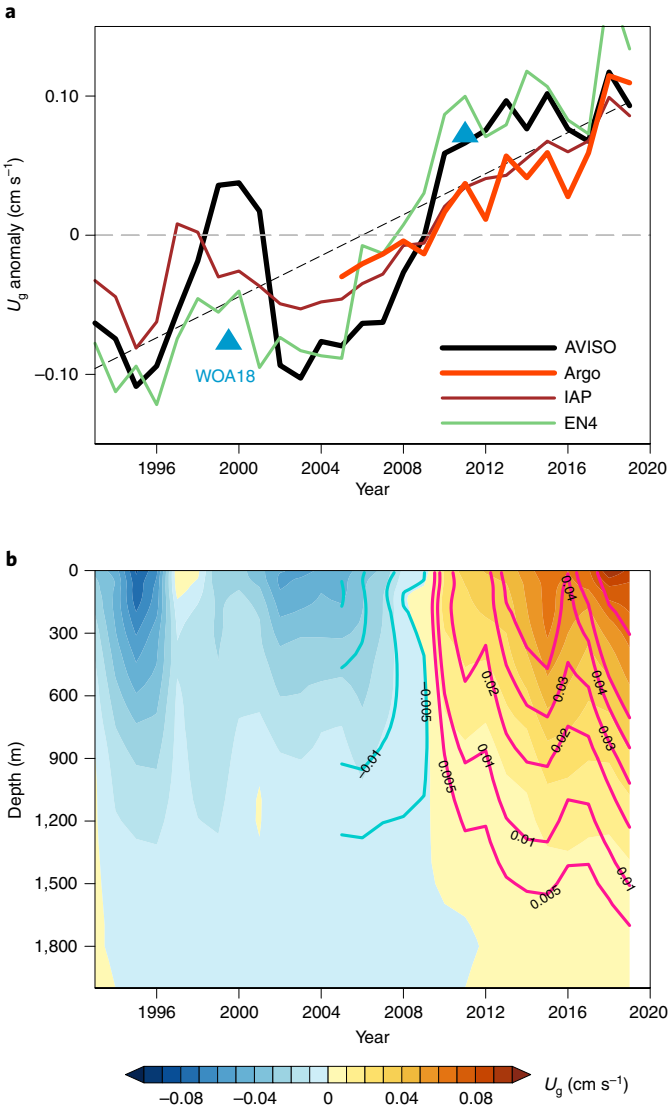

Fig. 2 | Time series of the observed zonal geostrophic velocity averaged between 48° S–58° S. a, Time series of observed surface zonal geostrophic velocity U_g anomaly from: AVISO (black), IAP (brown), EN4 (green) and Argo (red; since 2005). The blue triangles are decadal averages of U_g anomaly from WOA18. The dashed black line shows the linear trend of AVISO. U_g from ocean measurements are relative to 2,000 m depth. **b**, Hovmöller diagram of U_g (cm s^{-1}) anomaly from IAP (shading) and Argo (contours).

acceleration emerged from the background variability only during the recent decade.

For longer periods, the evidence for acceleration is even stronger. The trend in U_g from IAP for 1979–2019 (Fig. 4a) is similar to the Argo trend (Fig. 1d). Maximum warming is located north of 50° S (Extended Data Fig. 2a). South of the maximum warming, eastward zonal flow is intensified with stronger vertical shear. North of the maximum warming, negative change (weakened eastward or intensified westward flow) occurs along the boundary between eastward and westward flows, suggesting a southward shift of zonal flow and intensification of the zonally averaged subtropical gyres consistent with previous indications of subtropical gyre intensification[6,7,24]. To quantify the net acceleration of eastward flow, we calculate the eastward baroclinic transport in the upper 2,000 m based on IAP since 1940 (Supplementary Fig. 1). For all regions of eastward flow, the net intensification is about 2 Sv for 1940–2019.

The consistency across different observational datasets and analyses suggests a robust increase in zonally averaged eastward flow in the latitude band 48° S–58° S, associated with strongest warming north of the ACC and weak warming within and south of the ACC. We note that this latitude band is mostly north of Drake Passage and that the causative heating distribution is also north of Drake Passage. Hence this acceleration response to heating is weak in Drake Passage, where much of the trend analysis of the ACC has been carried out[20]. As a caveat, the Southern Ocean is subject to strong internal climate variability and the observations are sparse. We turn to numerical climate model simulations to corroborate the acceleration and for attribution of the physical mechanisms.

Mechanism for acceleration of flow using climate models

Acceleration of Southern Ocean zonal flow appears also in multiple climate model simulations that are subjected to anthropogenic forcing. We first use the multi-model mean (MMM) of 21 CMIP6 historical and SSP585 simulations. For comparison with observations, the difference between the zonal velocity in the upper 100 m and at 2,000 m depth, averaged between 48° S and 58° S, shows a long-term linear trend of 0.45 ± 0.33 cm s^{-1} per century for 1993–2019 (Fig. 3c). To test the sensitivity of this result to our practical use of a level of no motion (LNM) at 2,000 m for the observations, we examine the modelled velocity change at 2,000 m and the difference in transport between using the full velocity and a 2,000 m LNM in models. We find that modelled velocity changes at 2,000 m are insignificant and much smaller than the changes in the upper layer (Extended Data Fig. 3). Moreover, the baroclinic transport in the upper 2,000 m with no motion at 2,000 m dominates the change in the total transport with a very similar meridional structure (Extended Data Fig. 4a). Transports of both the eastward flow, centred at 50° S, and westward flow, centred at 39° S, intensify by around 3 Sv from 1955 to 2035 (Supplementary Fig. 2). This indicates a substantial spin-up of the subtropical gyre. Overall, the practical choice of an LNM at 2,000 m does not have a major impact on these trends.

Internal climate variability and model structural difference create large inter-model variability in CMIP6 (ref. [36]) (Fig. 3a,c). To separate internal from forced variability, we use large ensemble simulations[37,38] to interpret the observed structure. The meridional structures in ensemble mean are similar to the observed AVISO trend (Supplementary Fig. 3), supporting our hypothesis that the observed eastward acceleration is of anthropogenic origin. This, along with the result that the CESM1 Large Ensemble (LENS) mean trend is larger than the uncertainty (0.44 ± 0.16 cm s^{-1} per century for 1993–2019), leads us to conclude that the forced change has exceeded internal variability for the altimeter era. AVISO data alone may not fully justify the conclusion, but the agreement among models and with observations greatly strengthens the case.

The observed zonal velocity change since 1993 includes not only a trend but a large decadal oscillation through 2010 (Fig. 2a). This oscillation is not present in the multi-model mean, which suggests that it is internal variability. Individual LENS runs (for example, thin red curve in Fig. 3b) exhibit the forced response with internal variability that is similar in magnitude to the observed oscillation. The observed trends seem larger than model ensemble mean results within the uncertainty due to internal variability (Fig. 3c). For a longer period, since 1979 when the zonal velocity started climbing from a relatively stable state, the forced signal is more evident as the effect of internal variability weakens. Hence the longer-period observed trend is much closer to the ensemble mean results from CMIP6 and LENS (Fig. 3d).

Does model resolution matter? The models considered thus far are 'standard' resolution (about 1°) with eddy parameterizations and capture the observed maximum warming around 45° S and zonal velocity acceleration around 50° S (Fig. 4b). Comparison of a standard resolution CESM1-SR with the eddy-resolving CESM1-HR

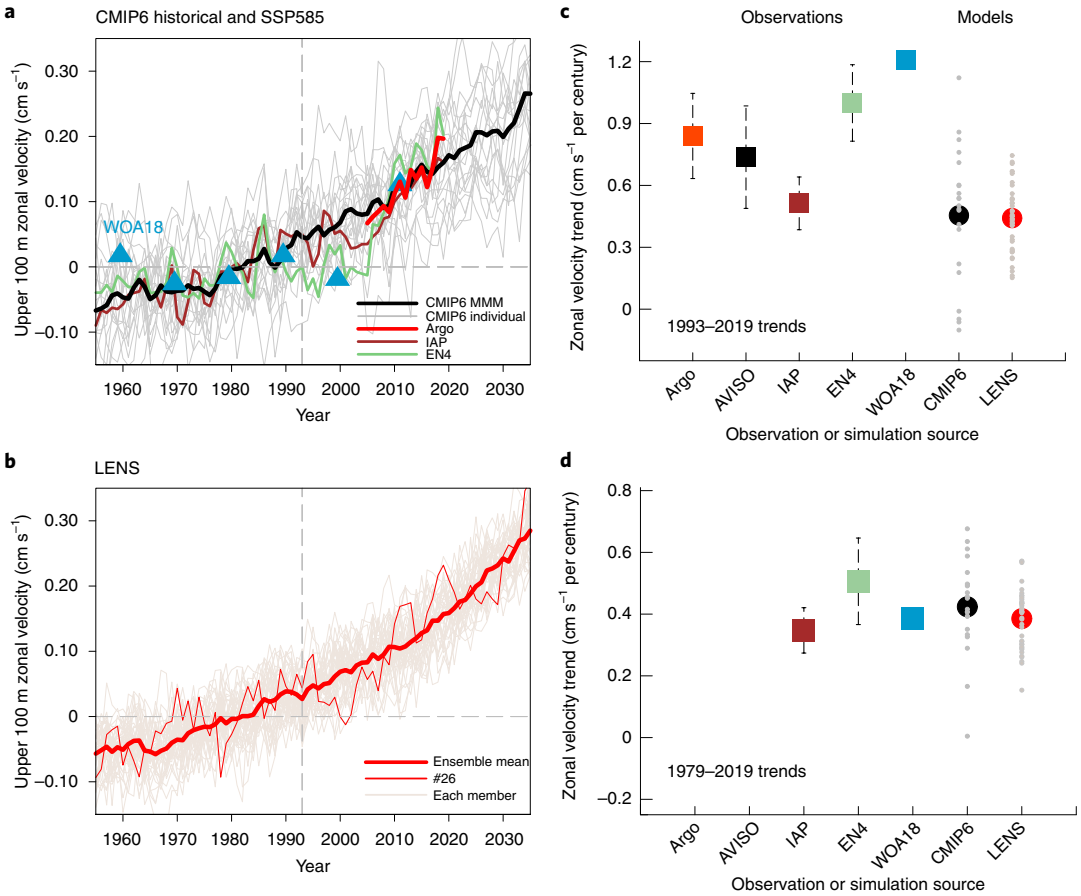

Fig. 3 | Comparison between the observed and simulated time series and trends of zonal velocity averaged between 48° S–58° S. a, Time series of upper 100 m zonal velocity (minus 2,000 m velocity) relative to the average of 1955–2004 from CMIP6 historical simulations. CMIP6 MMM is the black curve, with superimposed observation-based products: IAP (brown), EN4 (green), WOA18 (blue triangle) and Argo (red; since 2005). **b**, Time series of upper 100 m zonal velocity relative to the velocity at 2,000 m depth from LENS. LENS ensemble mean is shown as the thick red curve and an individual run is shown as the thin red curve. **c**, Trend of zonal velocity from observations (squares) and simulations (circles) in **a** and **b** from 1993 to 2019. For Argo, the trend is for 2005–2019. For CMIP6 runs, the trend is for 1993–2019. The error bar represents the 95% confidence interval for the linear trend. For WOA18, the changing rate is estimated based on the difference between 2005–2017 and 1995–2004 and then divided by 12 years. Small dots are results from individual runs from CMIP6 and LENS. **d**, Same as **c** but for the trend from 1979 to 2019.

(Methods) shows that the trends for 1979–2019 (Fig. 4c,d) and time evolution of zonal velocity (Supplementary Fig. 4) are similar. The small difference in trend is partly attributed to large internal variability, as shown by LENS. Thus, the eddy parameterizations in the standard resolution ocean models effectively reflect eddy activity under global warming.

Previous studies focused on wind effects on Southern Ocean climate change[19,20]. To compare buoyancy and wind-forcing changes, we define two indices: (1) the index 'ΔT' of buoyancy change is the zonal-mean upper 2,000 m temperature difference between 45° S and 60° S, latitudes where the maximum and minimum of warming occur, respectively; (2) the index 'SAM' of wind-stress change is the zonal-mean atmospheric surface pressure difference between 40° S and 65° S, which is the Southern Annular Mode index[39]. Across the CMIP6 models, the correlation coefficient between the 1979–2014 trends of ΔT and zonal flow change over the upper 100 m (ΔU) is 0.71, which is much larger than the correlation of 0.16 between the trends of SAM and ΔU (Extended Data Fig. 5). This demonstrates that ΔU is largely associated with the meridional gradient of ocean buoyancy change rather than wind stress change.

To further compare surface warming versus wind effects, we performed idealized experiments with two GCMs: the air–sea coupled CESM1 and the ocean-only MITgcm model (Methods). The buoyancy experiment from CESM1 (CESM1_ΔBuoy) largely reproduces the zonal-mean velocity trend from observations and CMIP6 (Fig. 4e). This result was confirmed with the buoyancy experiment from the ocean-only MITgcm (MITgcm_ΔSST). It captures the principal features from observations, CMIP6 and CESM1_ΔBuoy (Fig. 4f).

Idealized simulations with surface wind-stress changes show only small velocity changes (Extended Data Fig. 6) compared with those driven by SST change. Moreover, the wind-change-induced responses show maximum zonal flow change at mid-depth, unlike the surface-intensified flow change in observations, CMIP6 historical runs and the buoyancy-forcing experiments.

Overall, both sets of idealized simulation results suggest that acceleration of zonal flow in the Southern Ocean is a general feature of the ocean's response to surface warming and that wind changes play a secondary role in shaping the Southern Ocean response.

Spatial structure of Southern Ocean velocity response

If viewed only as a zonal mean, acceleration of the zonal flow and associated temperature changes might be interpreted as the intensification of a zonally oriented ACC at all longitudes. However, the accelerations/decelerations are localized to different parts of the Southern Ocean's zonal flows (Fig. 5). The strongest mean flows from AVISO data follow the Subantarctic Front (SAF), which is the

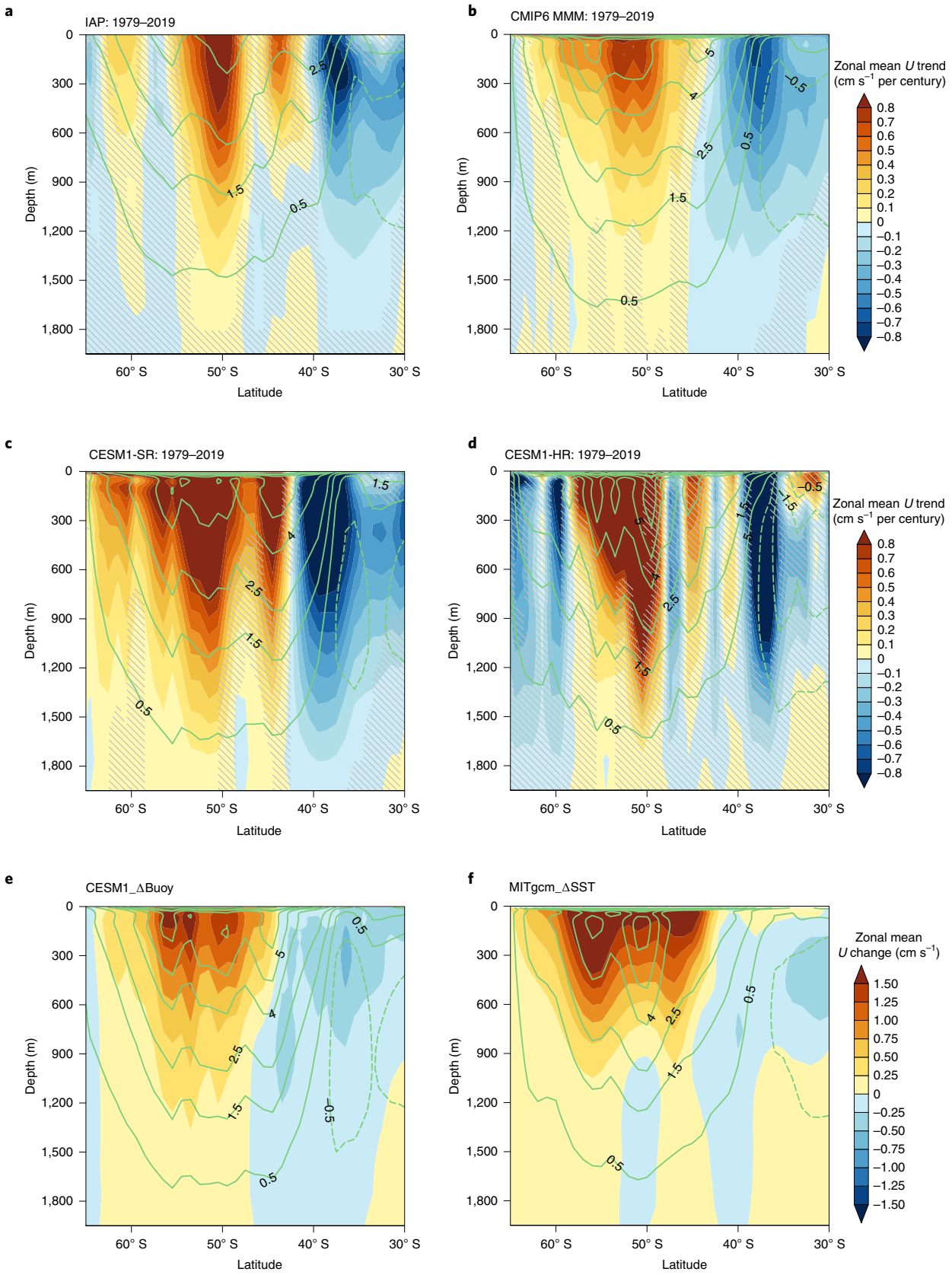

Fig. 4 | Zonal mean patterns of zonal velocity trend/change from observations and models. a–d, Zonal mean U (U_g for observations) trend from observations: IAP (**a**); and models: CMIP6 MMM (**b**), CESM1-SR (**c**) and CESM1-HR (**d**) from 1979 to 2019. **e**, Zonal mean U change from the CESM1_ΔBuoy experiment relative to the control run, averaged over 50 years. **f**, Zonal mean U change from the MITgcm_ΔSST experiment relative to the control run. All velocity changes from model simulations are relative to the velocity at 2,000 m depth. Green contours are the climatological U_g or U (in cm s^{-1}) from the corresponding cases. Hatched regions indicate that trends are not significant at the 95% confidence level.

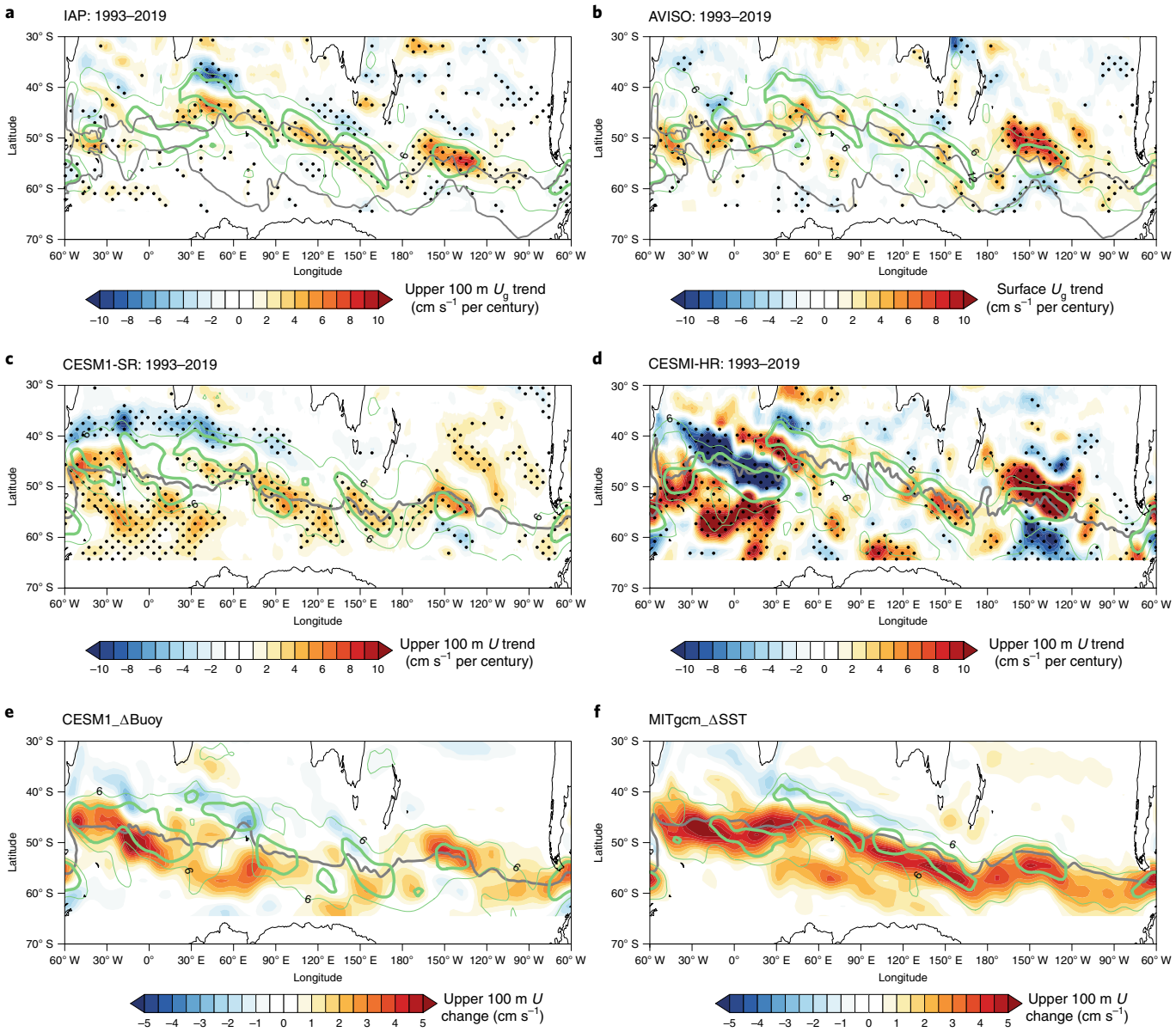

Fig. 5 | Spatial patterns of zonal velocity trend/change from observations and models. a, Upper 100 m U_g trend from IAP (1993–2019). Green contours indicate the Subantarctic Front and Southern ACC Front from north to south[46]. **b**, Surface U_g trend from AVISO (1993–2019). **c**,**d**, Upper 100 m U trend from CESM1-SR (1° resolution; **c**) and CESM1-HR (0.1° resolution; **d**). **e**,**f**, Upper 100 m U change from the CESM1_ΔBuoy experiment (**e**) and the MITgcm_ΔSST experiment (**f**) relative to their corresponding control runs. The grey curves in **c**–**f** are the defined 'SAF' based on the corresponding sea-surface height (Methods). Mean zonal velocities of 6 cm s^{-1} and 12 cm s^{-1} are shown as thin and thick green contours, respectively. Stippling indicates regions exceeding 90% statistical significance computed from the two-tailed t test.

northern boundary of the ACC, and the Agulhas Return Current. Observed eastward zonal flow acceleration has occurred mainly along the tilted SAF and Agulhas Return Current (Fig. 5a,b), whose latitudes vary from 40° S to 60° S. There is a slight negative trend (westward acceleration) north of and along the SAF in the Atlantic and eastern Indian oceans, suggesting a poleward shift of the SAF. The maximum SAF acceleration in the Pacific sector might be associated with spin-up of the subtropical gyre[6,7,24,25,40], but is probably natural variability based on the ensemble-mean result from LENS (Supplementary Fig. 5). To account for the meridional meanders of the ACC, we defined the 'SAF' based on the northernmost sea-surface-height contour passing through the Drake Passage and calculated the streamwise mean (Methods). In both the observed and simulated streamwise mean, the eastward acceleration occurs on both sides of the 'SAF', that is, within and to the north of the ACC. This pattern of eastward acceleration is associated with the ocean warming pattern displaced north of the ACC due to the upwelling damping within the ACC. The ocean warming is due to anthropogenic heat, which is modified by but cannot be removed by ocean eddies. We note that the ACC does not accelerate in Drake Passage in observations for 1993–2019 (Fig. 5a,b). We suggest that the eastward accelerations centred on the 'SAF' are associated with a spin-up and poleward shift of the subtropical gyre as implied by the westward current anomalies further to the north (Extended Data Figs. 7,8). The eastward acceleration remains centred on the 'SAF' even when the small 'SAF' shifts during different periods are considered in calculating the streamwise mean (Supplementary Fig. 6).

The three observational products covering longer periods also show SAF-intensification (Extended Data Fig. 9). The potential density trends are dominated by temperature trends. The most zonally coherent accelerations have meridional dipole structure and are strongest in longitudinal sectors where the subtropical temperature trends are strongest.

The CESM1-SR model velocity trend for 1993–2019 is similar to AVISO observations, with a meridional dipolar change in the Atlantic and Indian sectors (Fig. 5c). Although the zonal means in CESM1-SR and CESM1-HR are similar, the horizontal structure is sensitive to ocean model resolution: the magnitude and regional pattern from CESM1-HR are larger and more concentrated where ocean jets are stronger (Fig. 5d) compared with CESM1-SR (Fig. 5c). Here we see that the horizontal warming patterns in both observations and models (Extended Data Fig. 10) are tightly linked with velocity change patterns (Fig. 5).

The idealized buoyancy-driven GCM experiments (Fig. 5e,f) show the eastward accelerations mostly on the northern flank of the ACC, linked to the maximum ΔOHC, and mainly along the ocean fronts. The modelled acceleration is stronger and to the south of the observed. The current change in the Drake Passage, inconsistent with observations, remains to be investigated and could be due to strong warming in these experiments. For comparison, the wind-change-driven GCM experiments accelerate eastward flow much farther to the south and are much patchier (Extended Data Fig. 6e,f).

Summary and discussion

We find statistically significant acceleration of Southern Ocean zonal flow in the upper ocean between 48° S and 58° S, based on satellite altimeter and hydrographic data since 1993 and supported by multi-decadal hydrographic data analyses reaching back to 1979. The observed buildup in heat north of the ACC most likely caused the observed acceleration. Multiple model simulations and idealized experiments support attribution of the acceleration to the warming distribution, while wind change plays only a secondary role in the acceleration. We suggest that the negligible Southern Ocean current changes reported previously are the consequence of (1) the short observational record[2] and/or (2) the focus on the ACC transport through the Drake Passage[41–45], where the observed acceleration is weak (Fig. 5a,b). Guided by the model ensemble, the observed acceleration has just emerged, centred on the SAF on the northern flank of the ACC and in subtropical regions, associated with the spin-up and poleward shift of subtropical gyres, and is now distinguishable from the decadal variability. Given the continuing role of the Southern Ocean in oceanic heat uptake[11] and equatorward heat transport, we expect the zonal acceleration to continue and even increase, facilitating property exchange between ocean sectors and increasing ventilation of the subtropical thermocline as water moves along the accelerating SAF and enters the gyres. Further studies are needed to explore how the subtropical gyres, bathymetry, standing meanders and deep-mixed-layer distribution affect the regional or sectoral distribution of the greatest warming north of the ACC and the associated ocean current changes.

Online content

Any methods, additional references, Nature Research reporting summaries, source data, extended data, supplementary information, acknowledgements, peer review information; details of author contributions and competing interests; and statements of data and code availability are available at https://doi.org/10.1038/s41558-021-01212-5.

Received: 14 February 2021; Accepted: 6 October 2021;
Published online: 29 November 2021

References

1. Gille, S. T. Decadal-scale temperature trends in the Southern Hemisphere ocean. *J. Clim.* **21**, 4749–4765 (2008).
2. Böning, C. W., Dispert, A., Visbeck, M., Rintoul, S. R. & Schwarzkopf, F. U. The response of the Antarctic Circumpolar Current to recent climate change. *Nat. Geosci.* **1**, 864–869 (2008).
3. Roemmich, D. et al. Unabated planetary warming and its ocean structure since 2006. *Nat. Clim. Change* **5**, 240–245 (2015).
4. Durack, P. J. & Wijffels, S. E. Fifty-year trends in global ocean salinities and their relationship to broad-scale warming. *J. Clim.* **23**, 4342–4362 (2010).
5. Sabine, C. L. The oceanic sink for anthropogenic CO_2. *Science* **305**, 367–371 (2004).
6. Talley, L. D. et al. Changes in ocean heat, carbon content, and ventilation: a review of the first decade of GO-SHIP global repeat hydrography. *Annu. Rev. Mar. Sci.* **8**, 185–215 (2016).
7. Waugh, D. W., Primeau, F., DeVries, T. & Holzer, M. Recent changes in the ventilation of the southern oceans. *Science* **339**, 568–570 (2013).
8. Fyfe, J. C. Southern Ocean warming due to human influence. *Geophys. Res. Lett.* **33**, L19701 (2006).
9. Sigmond, M., Reader, M. C., Fyfe, J. C. & Gillett, N. P. Drivers of past and future Southern Ocean change: stratospheric ozone versus greenhouse gas impacts. *Geophys. Res. Lett.* **38**, L12601 (2011).
10. Swart, N. C., Gille, S. T., Fyfe, J. C. & Gillett, N. P. Recent Southern Ocean warming and freshening driven by greenhouse gas emissions and ozone depletion. *Nat. Geosci.* **11**, 836–841 (2018).
11. Shi, J.-R., Xie, S.-P. & Talley, L. D. Evolving relative importance of the Southern Ocean and North Atlantic in anthropogenic ocean heat uptake. *J. Clim.* **31**, 7459–7479 (2018).
12. Manabe, S., Bryan, K. & Spelman, M. J. Transient response of a global ocean–atmosphere model to a doubling of atmospheric carbon dioxide. *J. Phys. Oceanogr.* **20**, 722–749 (1990).
13. Armour, K. C., Marshall, J., Scott, J. R., Donohoe, A. & Newsom, E. R. Southern Ocean warming delayed by circumpolar upwelling and equatorward transport. *Nat. Geosci.* **9**, 549–554 (2016).
14. Shi, J.-R., Talley, L. D., Xie, S.-P., Liu, W. & Gille, S. T. Effects of buoyancy and wind forcing on Southern Ocean climate change. *J. Clim.* **33**, 10003–10020 (2020).
15. Rintoul, S. R. The global influence of localized dynamics in the Southern Ocean. *Nature* **558**, 209–218 (2018).
16. Hallberg, R. & Gnanadesikan, A. The role of eddies in determining the structure and response of the wind-driven Southern Hemisphere overturning: results from the Modeling Eddies in the Southern Ocean (MESO) project. *J. Phys. Oceanogr.* **36**, 2232–2252 (2006).
17. Meredith, M. P. & Hogg, A. M. Circumpolar response of Southern Ocean eddy activity to a change in the Southern Annular Mode. *Geophys. Res. Lett.* **33**, L16608 (2006).
18. Farneti, R., Delworth, T. L., Rosati, A. J., Griffies, S. M. & Zeng, F. The role of mesoscale eddies in the rectification of the Southern Ocean response to climate change. *J. Phys. Oceanogr.* **40**, 1539–1557 (2010).
19. Downes, S. M., Budnick, A. S., Sarmiento, J. L. & Farneti, R. Impacts of wind stress on the Antarctic Circumpolar Current fronts and associated subduction. *Geophys. Res. Lett.* **38**, L11605 (2011).
20. Meredith, M. P., Naveira Garabato, A. C., Hogg, A. M. & Farneti, R. Sensitivity of the overturning circulation in the Southern Ocean to decadal changes in wind forcing. *J. Clim.* **25**, 99–110 (2012).
21. Marshall, D. P., Ambaum, M. H. P., Maddison, J. R., Munday, D. R. & Novak, L. Eddy saturation and frictional control of the Antarctic Circumpolar Current. *Geophys. Res. Lett.* **44**, 286–292 (2017).
22. Hogg, A. M. et al. Recent trends in the Southern Ocean eddy field. *J. Geophys. Res. Oceans* **120**, 257–267 (2015).
23. Munday, D. R., Johnson, H. L. & Marshall, D. P. Eddy saturation of equilibrated circumpolar currents. *J. Phys. Oceanogr.* **43**, 507–532 (2013).
24. Roemmich, D. et al. Decadal spinup of the South Pacific subtropical gyre. *J. Phys. Oceanogr.* **37**, 162–173 (2007).
25. Fine, R. A., Peacock, S., Maltrud, M. E. & Bryan, F. O. A new look at ocean ventilation time scales and their uncertainties. *J. Geophys. Res. Oceans* **122**, 3771–3798 (2017).
26. Hu, S. et al. Deep-reaching acceleration of global mean ocean circulation over the past two decades. *Sci. Adv.* **6**, eaax7727 (2020).
27. Gent, P. R., Large, W. G. & Bryan, F. O. What sets the mean transport through Drake Passage? *J. Geophys. Res. Oceans* **106**, 2693–2712 (2001).
28. Borowski, D., Gerdes, R. & Olbers, D. Thermohaline and wind forcing of a circumpolar channel with blocked geostrophic contours. *J. Phys. Oceanogr.* **32**, 2520–2540 (2002).
29. Hogg, A. M. C. An Antarctic Circumpolar Current driven by surface buoyancy forcing. *Geophys. Res. Lett.* **37**, L23601 (2010).
30. Wang, G., Xie, S. P., Huang, R. X. & Chen, C. Robust warming pattern of global subtropical oceans and its mechanism. *J. Clim.* **28**, 8574–8584 (2015).

31. Hogg, A. M. C. & Gayen, B. Ocean gyres driven by surface buoyancy forcing. *Geophys. Res. Lett.* **47**, e2020GL088539 (2020).
32. Gent, P. R. & Mcwilliams, J. C. Isopycnal mixing in ocean circulation models. *J. Phys. Oceanogr.* **20**, 150–155 (1990).
33. Gent, P. R. & Danabasoglu, G. Response to increasing Southern Hemisphere winds in CCSM4. *J. Clim.* **24**, 4992–4998 (2011).
34. Liu, W. et al. Southern Ocean heat uptake, redistribution, and storage in a warming climate: the role of meridional overturning circulation. *J. Clim.* **31**, 4727–4743 (2018).
35. Roemmich, D. & Gilson, J. The 2004–2008 mean and annual cycle of temperature, salinity, and steric height in the global ocean from the Argo program. *Prog. Oceanogr.* **82**, 81–100 (2009).
36. Deser, C., Phillips, A., Bourdette, V. & Teng, H. Uncertainty in climate change projections: the role of internal variability. *Clim. Dyn.* **38**, 527–546 (2012).
37. Kay, J. E. et al. The Community Earth System Model (CESM) large ensemble project: a community resource for studying climate change in the presence of internal climate variability. *Bull. Am. Meteorol. Soc.* **96**, 1333–1349 (2015).
38. Swart, N. C. et al. The Canadian Earth System Model version 5 (CanESM5.0.3). *Geosci. Model Dev. Discuss.* **12**, 4823–4873 (2019).
39. Marshall, G. J. Trends in the Southern Annular Mode from observations and reanalyses. *J. Clim.* **16**, 4134–4143 (2003).
40. McDonagh, E. L. et al. Decadal changes in the South Indian Ocean thermocline. *J. Clim.* **18**, 1575–1590 (2005).
41. Chidichimo, M. P., Donohue, K. A., Watts, D. R. & Tracey, K. L. Baroclinic transport time series of the Antarctic Circumpolar Current measured in Drake Passage. *J. Phys. Oceanogr.* **44**, 1829–1853 (2014).
42. Donohue, K. A., Tracey, K. L., Watts, D. R., Chidichimo, M. P. & Chereskin, T. K. Mean Antarctic Circumpolar Current transport measured in Drake Passage. *Geophys. Res. Lett.* **43**, 11760–11767 (2016).
43. Hughes, C. W., Williams, J., Coward, A. C. & de Cuevas, B. A. Antarctic circumpolar transport and the southern mode: a model investigation of interannual to decadal timescales. *Ocean Sci.* **10**, 215–225 (2014).
44. Killworth, P. D. & Hughes, C. W. The Antarctic Circumpolar Current as a free equivalent-barotropic jet. *J. Mar. Res.* **60**, 19–45 (2002).
45. Koenig, Z., Provost, C., Ferrari, R., Sennechael, N. & Rio, M.-H. Volume transport of the Antarctic Circumpolar Current: production and validation of a 20 year long time series obtained from in situ and satellite observations. *J. Geophys. Res. Oceans* **119**, 5407–5433 (2014).
46. Orsi, A. H., Whitworth, T. & Nowlin, W. D. On the meridional extent and fronts of the Antarctic Circumpolar Current. *Deep Sea Res. I* **42**, 641–673 (1995).

Methods

Observations. Satellite-based sea-surface heights (SSH) relative to the geoid (data from AVISO satellite altimetry) were used to investigate dynamic changes of the ocean surface. The surface geostrophic velocity is:

$$U_g\,(\text{surface}) = -\frac{g}{f}\frac{\partial \eta}{\partial y} \quad (1)$$

where η is the altimetric SSH, y represents the meridional direction, g is the acceleration due to gravity and f is the Coriolis parameter. The spatial resolution of the product is 1/4° (720 latitude × 1,440 longitude). Observed altimeter trends (1993–2019) were smoothed to spectral wavenumber 42 to remove higher frequencies from the field[47] and then remapped to 1°×1° for comparison with other observations.

The Argo programme, consisting of a global array of 3,800 free-drifting profiling floats, provides systematic coverage of global ocean temperature and salinity of the upper 2,000 m since 2005 (ref. [3]), before which the sampling was spatially and temporally sparse, especially in the Southern Hemisphere. Here we used the monthly gridded Argo temperature and salinity data[35] from 2005 to 2019 to examine recent trends and to compute dynamic height and geostrophic velocity relative to 2,000 dbar:

$$D = -\frac{1}{g}\int_{p_0}^{p}\frac{1}{\rho}\mathrm{d}p \quad (2)$$

$$U_g\,(p) - U_g\,(p_0) = -\frac{g}{f}\frac{\partial D}{\partial y} \quad (3)$$

where D is the dynamic height at pressure p relative to reference pressure p_0 and ρ is density. The relative zonal geostrophic velocity is the velocity relative to the velocity at the reference level, p_0. Although 2,000 dbar is not actually an LNM in the ACC, here we use it as a reference level of no motion, $U_g\,(p_0) = 0$, to compute the geostrophic shear. To validate the usage of LNM here, we show the 2,000 m velocity change from models, which is much smaller than the change in the upper layer (Extended Data Fig. 3). We also compute the absolute geostrophic velocity by using surface geostrophic velocity from AVISO as the reference (Extended Data Fig. 1). The data are on a 1°×1° grid with 58 vertical levels from the surface to 2,000 m.

IAP, EN4 and WOA18 datasets (temperature and salinity) were used to examine the trends of potential temperature and geostrophic velocity for longer periods. The calculation of geostrophic velocity is the same as that for Argo data (Equations (2) and (3)). These observationally based products include shipboard, mechanical bathythermograph, eXpendable BathyThermograph (XBT) and Argo profiles. IAP provides monthly mean ocean temperature and salinity from 1940 through 2019 (ref. [48]). The data are on a regular 1°×1° grid with 41 vertical depth levels in the upper 2,000 m. The data gaps are filled by the first-guess field from time-evolving outputs from an ensemble of Coupled Model Intercomparison Project 5 (CMIP5) models[49]. EN4 (version EN4.2.1) is a subsurface temperature and salinity dataset for the global oceans, spanning 1900 to 2019 with monthly timesteps[50]. The XBT bias was corrected using the methods from ref. [51]. The data are on a regular 1°×1° grid with 42 vertical depth levels in the upper 2,000 m. WOA18 is a uniformly formatted and quality-controlled dataset based on the World Ocean Database. Objectively analysed climatologies of temperature and salinity[52] (1955–1964, 1965–1974, 1975–1984, 1985–1994, 1995–2004 and 2005–2017) were used in this study to calculate geostrophic velocity for corresponding decades. To infill gaps, the first-guess field for each of these climatologies is from 'all-data', which is time-indeterminant[52]. It may contribute to the nearly constant zonal geostrophic velocity, compared with the results from the IAP data, before the Argo era (Fig. 3a). The data are on a 1°×1° grid from the surface to 5,350 m depth. Here we focus on the fields in the upper 2,000 m.

CMIP6 simulations. A set of CMIP6 historical and Shared Socioeconomic Pathway (SSP) 5-8.5 (SSP585) simulations[53], including solar, volcanic, anthropogenic aerosol, ozone depletion, land-use change and greenhouse gas effects, was used here. One of the advantages of CMIP6 compared with CMIP5 is that the CMIP6 historical simulation extends to the near present, the year 2014. We append SSP585 runs, which approximately follow Representative Concentration Pathway 8.5 (RCP8.5) scenarios global forcing pathway in CMIP5 with SSP5 socioeconomic conditions[54], to historical runs. Linear trends are calculated over different periods, such as 1979–2019 and 1993–2019, for ocean potential temperature and ocean zonal velocity. Velocity at 2,000 m depth is subtracted from the modelled velocity trends to be consistent with geostrophic velocity relative to 2,000 dbar calculated from observations. The results from the multi-model ensemble mean of 21 CMIP6 models represent the externally forced responses. Uncertainty ranges stated in the text are ±1 standard deviation across the models. The CMIP6 models used in this study for the ocean potential temperature and zonal velocity are listed in Supplementary Table 1. We regridded all model output to a regular 1°×1° latitude–longitude grid.

Streamwise mean. To separate the ACC regions and the subtropical gyres, we defined a 'Subantarctic Front' ('SAF') as the circumpolar sea-surface-height contour passing through the Drake Passage at the point 67.5° W, 57.5° S. It is the northernmost point where all CMIP6 model simulations have values. The so-defined 'SAF' is not based on the large SSH gradient, but it approximates the front location (green contours in Fig. 5). We then averaged the zonal velocity in the 'SAF'-following coordinate system. The streamwise coordinate covers the regions from 10° south to 10° north of the latitude of the 'SAF'. We then calculated the mean along the streamlines based on observations and model simulations. The results are not sensitive to the choice of this point close to the northern edge of the Drake Passage. In addition, the 'SAF' has been shifted poleward, but the magnitude is very small based on models: less than 0.2° in latitude in zonal mean from 1940–1960 to 1998–2018. Two 'SAF's at different periods were used to calculate the streamwise mean at corresponding periods. This method clearly separates the ACC and subtropical regions. We noted that it has limited utility with respect to quantifying the shifting effect on temperature responses precisely due to its small displacement in 'SAF' compared with the model grid.

Large ensemble simulations. We used two sets of large ensemble simulations: the CESM1 Large Ensemble (LENS) and the Canadian Earth System Model version 5 (CanESM5) large ensemble; CanESM5 is part of CMIP6. LENS includes 40 realizations that start with different initial conditions for the air temperature to drive ensemble spread, but with identical radiative forcing[37]. The effects of external forcing and internal climate variability can be isolated by analysing the ensemble mean and deviations, respectively. All the external anthropogenic and natural forcings are applied to force the fully coupled model following historical (1920–2005) and the RCP8.5 scenarios (2006–2100). Similarly, CanESM5 includes 25 members with different atmospheric initial conditions under historical (1850–2014) and future radiative-forcing scenarios (RCP8.5: 2015–2100)[38]. The linear trends are calculated for ocean zonal velocity and surface geostrophic velocity based on sea-surface height from these two sets of large ensemble simulations. Uncertainty ranges stated in the text are ±1 standard deviation across the realizations, representing the internal variability.

CESM high-resolution and standard-resolution simulations. The CESM high-resolution simulation (CESM1-HR or CESM1-CAM5-SE-HR) used in this study is version 1.3 at 0.25° resolution for the atmosphere and land and 0.1° resolution for the ocean and sea-ice components, performed under the umbrella of the International Laboratory for High-Resolution Earth System Prediction. The transient simulation with future extension as close to RCP8.5 as possible within CMIP6, spanning from 1950 to 2050, is part of the High-Resolution Model Intercomparison Project (HighResMIP)[55]. Mesoscale eddies in the ocean are resolved in CESM1-HR. To diagnose the sensitivity of our results to the model resolution, we also used CESM version 1.3 standard-resolution simulation (CESM1-SR or CESM1-CAM5-SE-LR) for comparison. The atmosphere and ocean model in CESM1-SR has an approximate grid spacing of about 1°, with other setups the same as CESM1-HR. The ocean model employs a temporally and spatially varying specification of the Gent–McWilliams eddy parameterization[32,33]. We investigated long-term trends of zonal velocity for 1979–2019 and 1993–2019 and discussed whether the parameterized and resolved mesoscale eddies affect our conclusions.

Idealized GCMs. Here we employed a partial coupling technique[56] to isolate the effects of the atmosphere-warming-induced and wind-change-induced Southern Ocean climate change. We used the CESM version 1.0.5, in which version 5 of the Community Atmosphere Model (CAM5) runs at a nominal 2° resolution (1.9° latitude × 2.5° longitude) with 26 vertical layers, and version 2 of Parallel Ocean Program (POP2) runs at a nominal resolution of 0.5° in latitude and 1° in longitude over the Southern Ocean. The Community Land Model, version 4, and Community Ice Code, version 4, are coupled with the atmosphere and ocean model. A temporally and spatially varying specification of the Gent–McWilliams eddy parameterization is employed in the ocean model. First, we ran a fully coupled, preindustrial control run (CTRL) as the baseline, which starts from the AD 1850 scenario. We then ran a simulation (CESM1_ΔBuoy) with the atmospheric CO_2 level quadrupled but prescribing the surface wind from CTRL. The transient response to surface buoyancy change can be obtained by taking the difference between CESM1_ΔBuoy and CTRL. To isolate the effect of the wind change under global warming, we also ran a simulation (CESM1_ΔWind) with the atmospheric CO_2 level quadrupled and prescribing the surface wind from a fully coupled, abruptly quadrupled CO_2 run. Sea surface temperature (SST) and sea surface salinity (SSS) interact with the atmosphere and evolve in time. Therefore, the responses to wind change can be obtained by taking the difference between CESM1_ΔWind and CESM1_ΔBuoy. More details about this CESM1 model configuration and setup can be found in ref. [34]. All of these cases were run for 90 years (Supplementary Table 2). The Southern Ocean zonal velocity and potential temperature shown are changes due to surface buoyancy and wind change over years 41–90.

We also used an ocean-only GCM to investigate the changes driven by surface warming and wind change. The ocean-only GCM utilized in this study is the Massachusetts Institute of Technology General Circulation Model (MITgcm). The model is based on the LLC90 grid[57] and the horizontal resolution is 1°×1/3° at low

and high latitudes and gradually changes to 1°×1° at midlatitudes. The model has 50 layers in the vertical direction, with the layer thicknesses ranging from 10 m at the surface to 456 m at the ocean bottom. Isopycnal diffusion and eddy-induced mixing were parameterized with the GM/Redi scheme[32,58]. The vertical mixing follows the GGL90 turbulent kinetic energy vertical-mixing scheme[59]. The initial state, as well as surface-forcing fields such as 6-hour zonal and meridional surface wind speed, 2-m air temperature and specific humidity, downward longwave and shortwave and precipitation, are obtained from the Estimating the Circulation and Climate of the Ocean Version 4 Release 4 (ECCO v4r4)[57]. The model is first integrated forward from 1 January 1992 to 31 December 2017. The monthly climatological SST, SSS, surface-wind stress and air–sea fluxes including surface net heat flux, surface net short wave flux and surface net freshwater flux are stored as new forcing fields. With these new forcing fields, the model is further integrated for 100 years to reach a quasi-equilibrium state. Variants of this configuration have been successfully used to address ocean dynamic and thermodynamic processes[60,61].

To assess the specific oceanic response to global warming-induced SST and wind-stress changes (denoted as Δ), we performed three experiments with the MITgcm (Supplementary Table 3). The multi-model (Supplementary Table 4) ensemble mean ΔSST and ΔWind used in the experiments are calculated as the years 100–140 mean difference between CMIP6 abrupt-4×CO_2 and pre-industrial control (piControl) experiments. Restarting from the spun-up solution of year 100, the three experiments are integrated forward an additional 140 years; the results shown in this study are the average of the last 40 years (100–140) of each experiment. In the control run (MITgcm_CTL), we forced the model using the present-day monthly climatological wind field (WindClim) and the SST and SSS are strongly restored to the current monthly climatological SST (SSTClim) and SSS (SSSClim). The restoring timescale is 10 days for SST (~50 W m^{-2} K for the 10 m upper layer) and SSS. The output of MITgcm_CTL is thus the ocean state forced by current forcing fields. In the MITgcm_ΔSST, the forcing fields are the same as MITgcm_CTL but SST is restored to the prescribed SSTClim + ΔSST. The difference, MITgcm_ΔSST minus MITgcm_CTL, yields the oceanic response to ΔSST induced by the increases of greenhouse gas concentrations. In the MITgcm_ΔWind, wind stress is restored to WindClim + ΔWind and SST/SSS are restored to SSTClim/SSSClim. The difference between MITgcm_ΔWind and MITgcm_CTL isolates the impacts of wind-stress change.

Data Availability

Argo data are available at: http://www.argo.ucsd.edu. IAP data are available at: https://climatedataguide.ucar.edu/climate-data/ ocean-temperature-analysis-and-heat-content- estimate-institute-atmospheric-physics. EN4 data are available at: https://www.metoffice.gov.uk/hadobs/en4/. WOA18 data are available at: https://www.nodc.noaa.gov/OC5/woa18/. Satellite altimetry data are available at: https://www.aviso.altimetry.fr/en/data.html. The CMIP6, CanESM5 large ensemble, CESM1-HR and CESM1-SR data are available on the Program for Climate Model Diagnostics and Intercomparison's Earth System Grid (https://esgf-node.llnl.gov/search/cmip6/). The CESM LENS simulations are available on the Earth System Grid (www.earthsystemgrid.org). The CESM and MITgcm model data used in this study are available from the corresponding author upon request.

References

47. Fasullo, J. T. & Nerem, R. S. Altimeter-era emergence of the patterns of forced sea-level rise in climate models and implications for the future. *Proc. Natl Acad. Sci. USA* **115**, 12944–12949 (2018).
48. Cheng, L., Wang, G., Abraham, J. & Huang, G. Decadal ocean heat redistribution since the late 1990s and its association with key climate modes. *Climate* **6**, 91 (2018).
49. Cheng, L. & Zhu, J. Benefits of CMIP5 multimodel ensemble in reconstructing historical ocean subsurface temperature variations. *J. Clim.* **29**, 5393–5416 (2016).
50. Good, S. A., Martin, M. J. & Rayner, N. A. EN4: quality controlled ocean temperature and salinity profiles and monthly objective analyses with uncertainty estimates. *J. Geophys. Res. Oceans* **118**, 6704–6716 (2013).
51. Gouretski, V. & Reseghetti, F. On depth and temperature biases in bathythermograph data: development of a new correction scheme based on analysis of a global ocean database. *Deep Sea Res. I* **57**, 812–833 (2010).
52. Locarnini, R. A. et al. *World Ocean Atlas 2018 Volume 1: Temperature* NOAA Atlas NESDIS 81 (Ocean Climate Laboratory National Centers for Environmental Information, 2019).
53. Eyring, V. et al. Overview of the Coupled Model Intercomparison Project phase 6 (CMIP6) experimental design and organization. *Geosci. Model Dev.* **9**, 1937–1958 (2016).
54. O'Neill, B. C. et al. The Scenario Model Intercomparison Project (ScenarioMIP) for CMIP6. *Geosci. Model Dev.* **9**, 3461–3482 (2016).
55. Haarsma, R. J. et al. High Resolution Model Intercomparison Project (HighResMIP v1.0) for CMIP6. *Geosci. Model Dev.* **9**, 4185–4208 (2016).
56. Liu, W., Lu, J. & Xie, S.-P. Understanding the Indian Ocean response to double CO_2 forcing in a coupled model. *Ocean Dyn.* **65**, 1037–1046 (2015).
57. Forget, G. et al. ECCO version 4: an integrated framework for non-linear inverse modeling and global ocean state estimation. *Geosci. Model Dev. Discuss.* **8**, 3653–3743 (2015).
58. Redi, M. H. Oceanic isopycnal mixing by coordinate rotation. *J. Phys. Oceanogr.* **12**, 1154–1158 (1982).
59. Gaspar, P., Grégoris, Y. & Lefevre, J.-M. A simple eddy kinetic energy model for simulations of the oceanic vertical mixing: tests at Station Papa and long-term upper ocean study site. *J. Geophys. Res. Oceans* **95**, 16179–16193 (1990).
60. Peng, Q., Xie, S. P., Wang, D., Zheng, X. T. & Zhang, H. Coupled ocean–atmosphere dynamics of the 2017 extreme coastal El Niño. *Nat. Commun.* **10**, 298 (2019).
61. Peng, Q. et al. Eastern Pacific wind effect on the evolution of El Niño: implications for ENSO diversity. *J. Clim.* **33**, 3197–3212 (2020).

Acknowledgements

We thank S. T. Gille, S. Sun and Y. Lu for enlightening discussions. J.-R.S. is supported by the US National Science Foundation (AGS-1637450) and the Southern Ocean Carbon and Climate Observations and Modeling project under National Science Foundation Award PLR-1425989. L.D.T. is also supported by the Southern Ocean Carbon and Climate Observations and Modeling project. Q.P. is supported by the National Natural Science Foundation of China (42005035). W.L. is supported by the Regents' Faculty Fellowship, Alfred P. Sloan Foundation Research Fellowship and US National Science Foundation (OCE-2123422).

Author contributions

J.-R.S. designed the research, analysed the data and wrote the paper. L.D.T. and S.-P.X. designed the research and wrote the paper. Q.P. and W.L. performed the experiment.

Competing interests

The authors declare no competing interests.

Additional information

Extended data is available for this paper at https://doi.org/10.1038/s41558-021-01212-5.

Supplementary information The online version contains supplementary material available at https://doi.org/10.1038/s41558-021-01212-5.

Correspondence and requests for materials should be addressed to Jia-Rui Shi.

Peer review information *Nature Climate Change* thanks Andrew Hogg and the other, anonymous, reviewer(s) for their contribution to the peer review of this work.

Reprints and permissions information is available at www.nature.com/reprints.

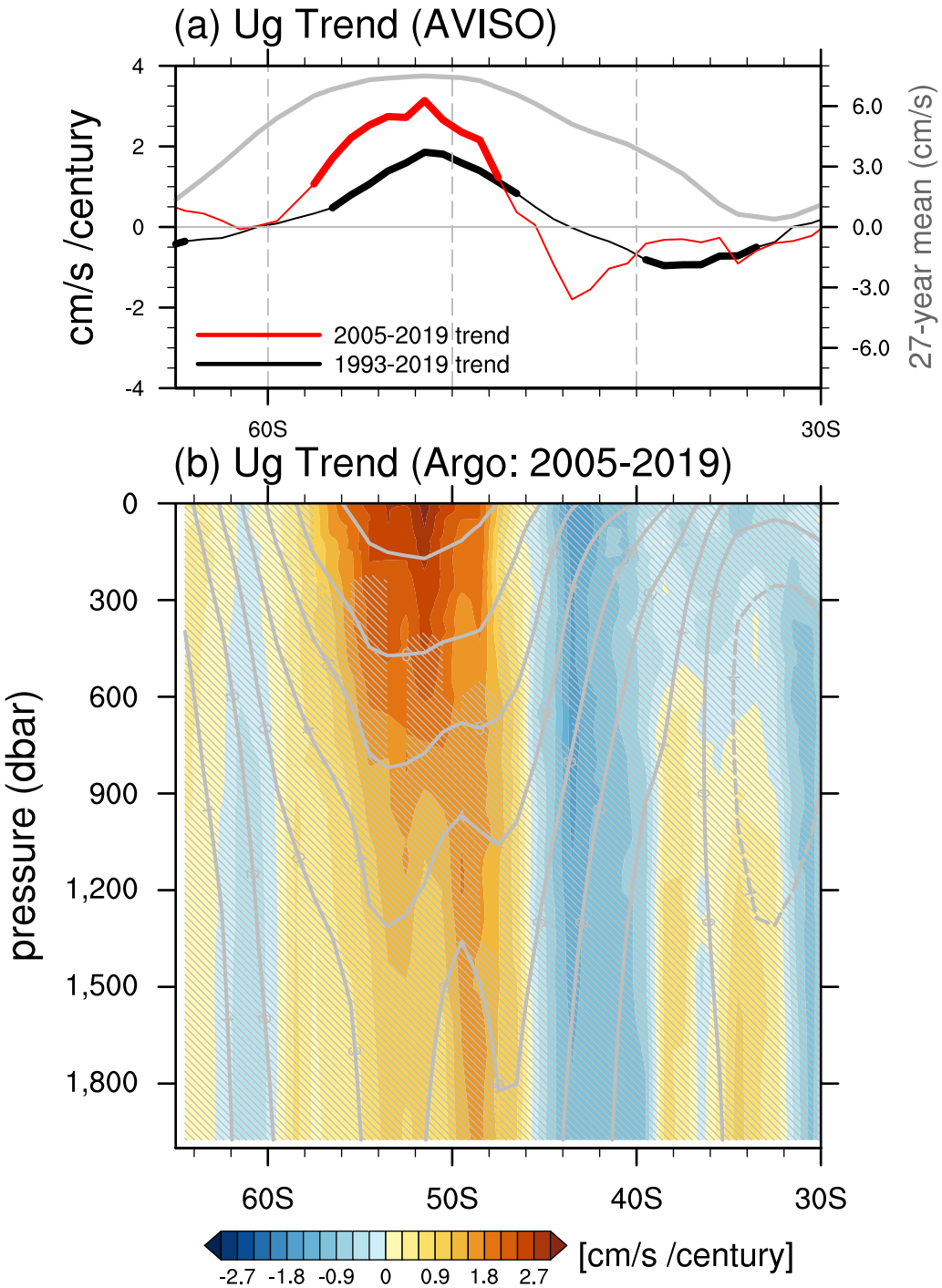

Extended Data Fig. 1 | Absolute geostrophic velocity trend from observations. (**a**) Ug from AVISO, same with Fig. 1c. (**b**) Zonal absolute geostrophic velocity (Ug) trend applying the surface AVISO-based Ug in (a) as a reference velocity. Gray contours are climatological absolute Ug, with solid contours representing eastward flow and dashed contours representing westward flow.

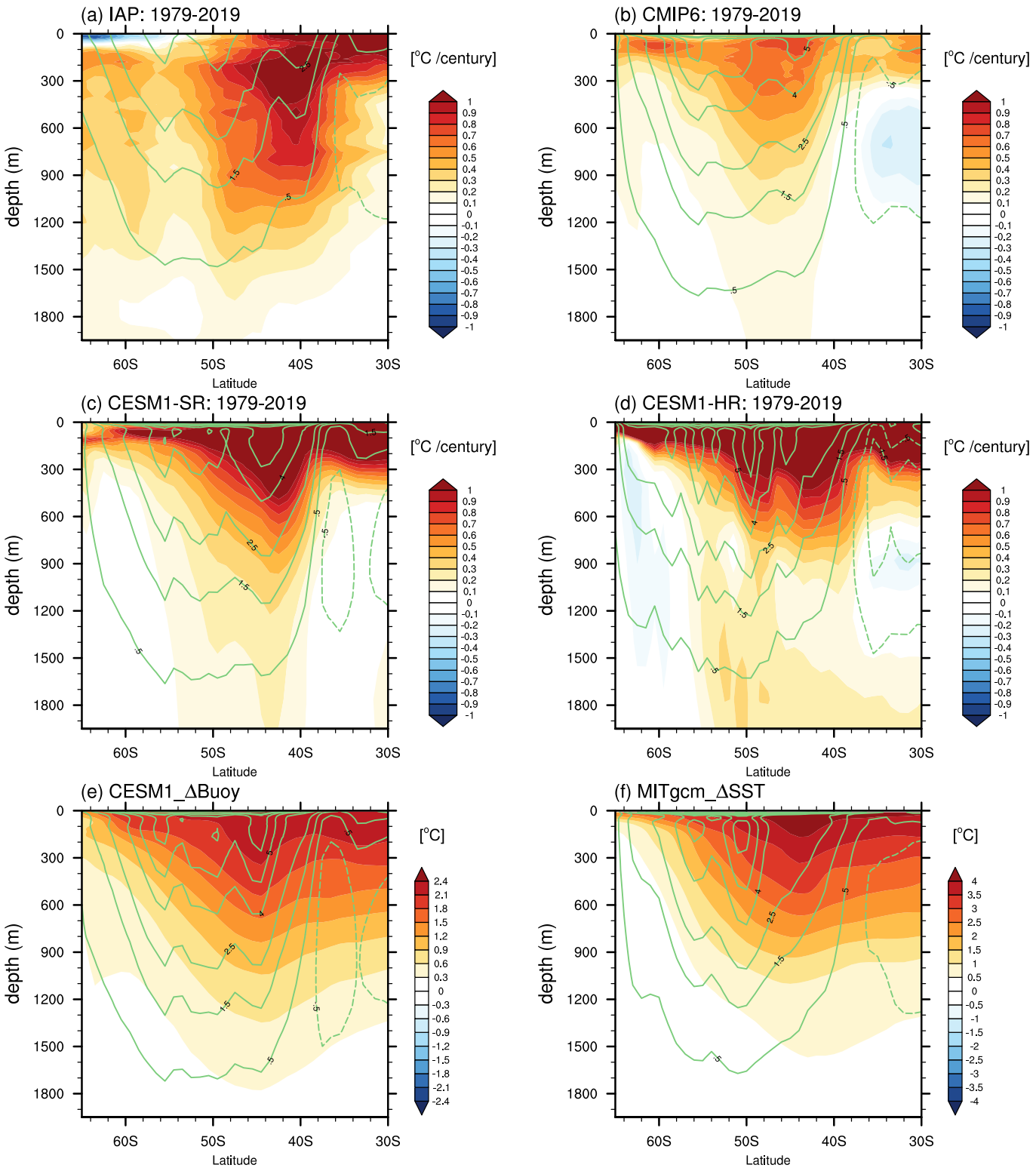

Extended Data Fig. 2 | Zonal mean patterns of potential temperature trend/change from observations and models. Potential temperature trend from 1979 to 2019 from (**a**) IAP (observations), (**b**) CMIP6 MMM, (**c**) CESM1-SR, and (**d**) CESM1-HR. (**e**) Zonal mean potential temperature change from the CESM1_ΔBuoy experiment relative to the control run. (**f**) Zonal mean potential temperature change from the MITgcm_ΔSST experiment relative to the control run. Green contours are the climatological Ug or U (in cm/s) from the corresponding cases.

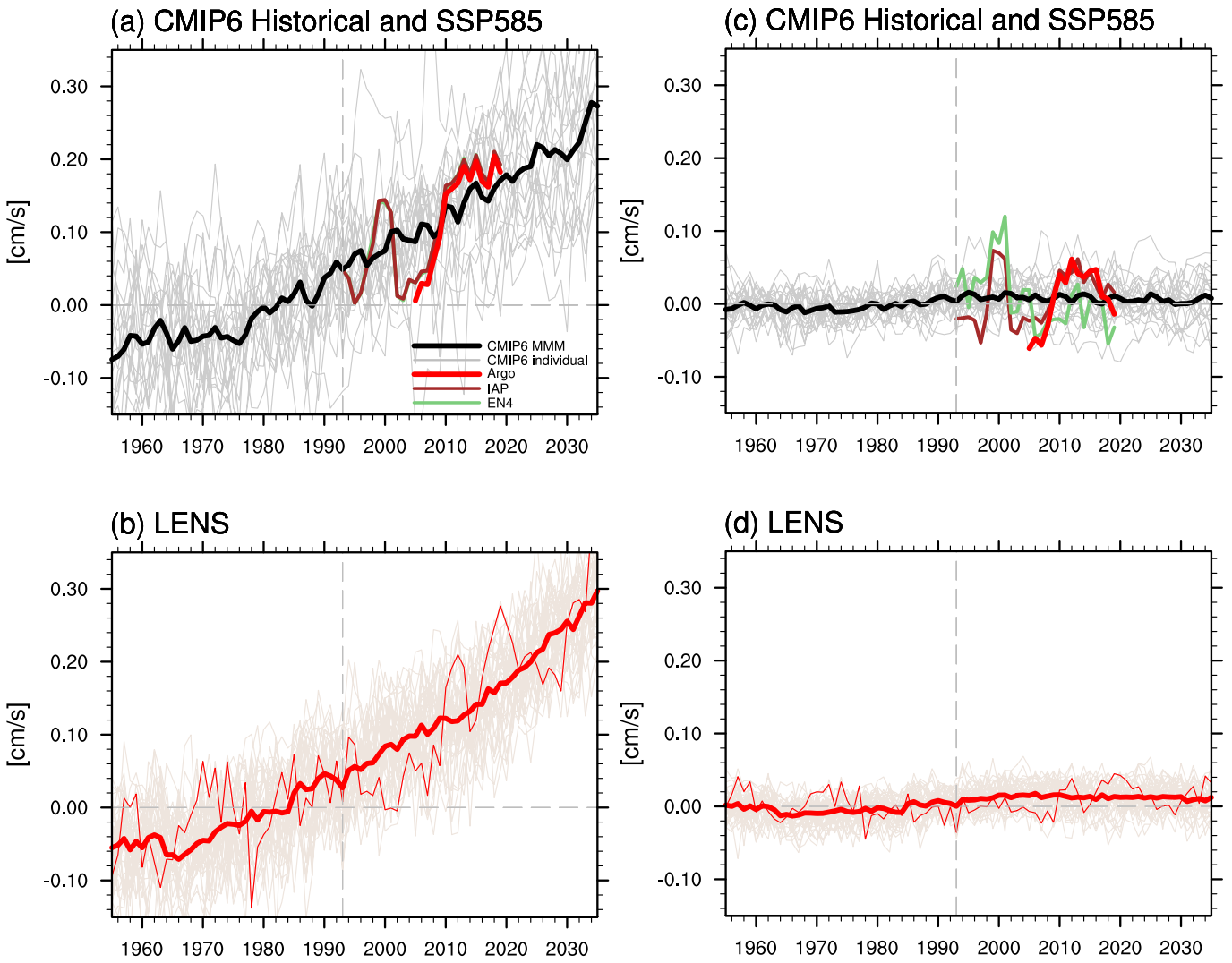

Extended Data Fig. 3 | Time series of upper 100 m and 2,000m zonal velocity. (**a**, **b**), Time series of upper 100 m zonal velocity averaged between 48°S-58°S relative to the average of 1955–2004 from CMIP6 and LENS simulations, respectively. CMIP6 multi-model mean (MMM) is the black curve, with superimposed observation-based products: IAP (brown), EN4 (green), and Argo (red; since 2005). The velocities from observation-based products apply the surface altimetry-based Ug as a reference velocity. (**c**, **d**), Same with (a, b), but for the 2,000 m zonal velocity.

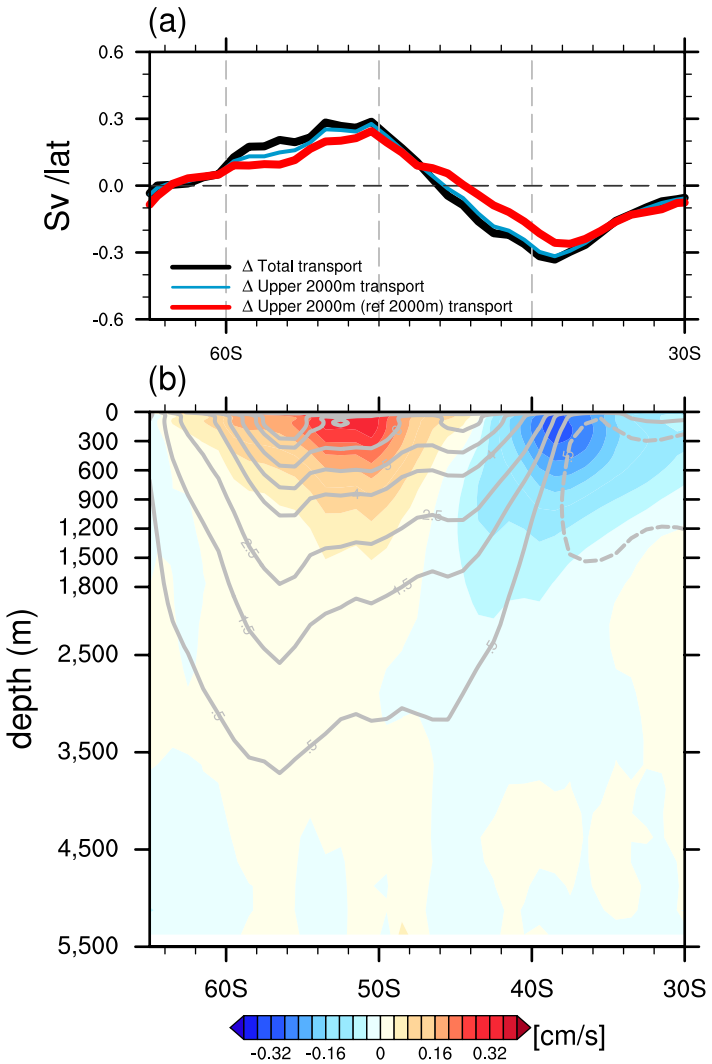

Extended Data Fig. 4 | Changes of zonal mean zonal velocity and transport from CMIP6. (**a**) Transport changes of zonal mean zonal velocity between 1995–2035 and 1955–1995 from CMIP6 MMM. Total transport change is shown as black curve, upper 2,000 m transport is shown as blue curve, and baroclinic transport with no motion at 2,000 m is shown as red curve. (**b**) Full-depth zonal velocity change between 1995–2035 and 1955–1995 from CMIP6 MMM. Gray contours are climatological zonal velocity, with solid contours representing eastward flow and dashed contours representing westward flow.

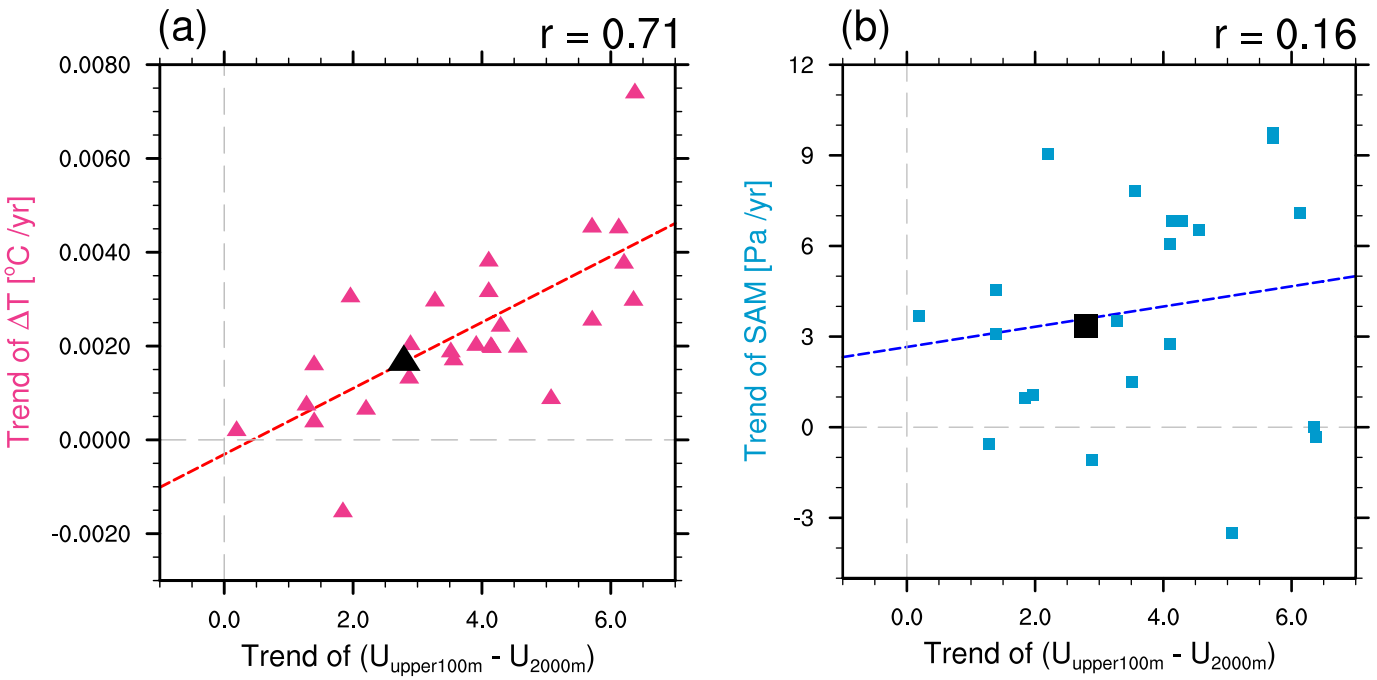

Extended Data Fig. 5 | Scatter plot of zonal velocity trend against temperature trend and against wind trend. (**a**) Scatter plot of trend (1979–2014) of upper 100 m zonal velocity relative to 2,000 m depth versus trend of temperature difference between 45°S and 60°S, along with the linear relationship for the CMIP6 models: BBC-CSM2-MR, BCC-ESM1, CAMS-CSM1-0, CanESM5, CAS-ESM2-0, CESM2, CESM2-FV2, CESM2-WACCM, CESM2-WACCM-FV2, CMCC-CM2-HR4, CMCC-CM2-SR5, EC-Earth3, EC-Earth3-Veg, FGOALS-g3, FIO-ESM-2-0, GFDL-CM4, GISS-E2-1-G, IPSL-CM6A-LR, MCM-UA-1-0, MIROC6, MPI-ESM1-1-2-HAM. MPI-ESM1-2-LR, MRI-ESM2-0, NESM3, SAM0-UNICON, and TaiESM1. Each red triangle indicates the result of each CMIP6 model. The correlation coefficient is 0.71 across models. The black triangle represents the trend from the IAP product. (**b**) Scatter plot of velocity trend versus SAM. Each blue square indicates the result from each CMIP6 model. The correlation coefficient is 0.16 across models. The black square represents the SAM trend from ERA5 (observations).

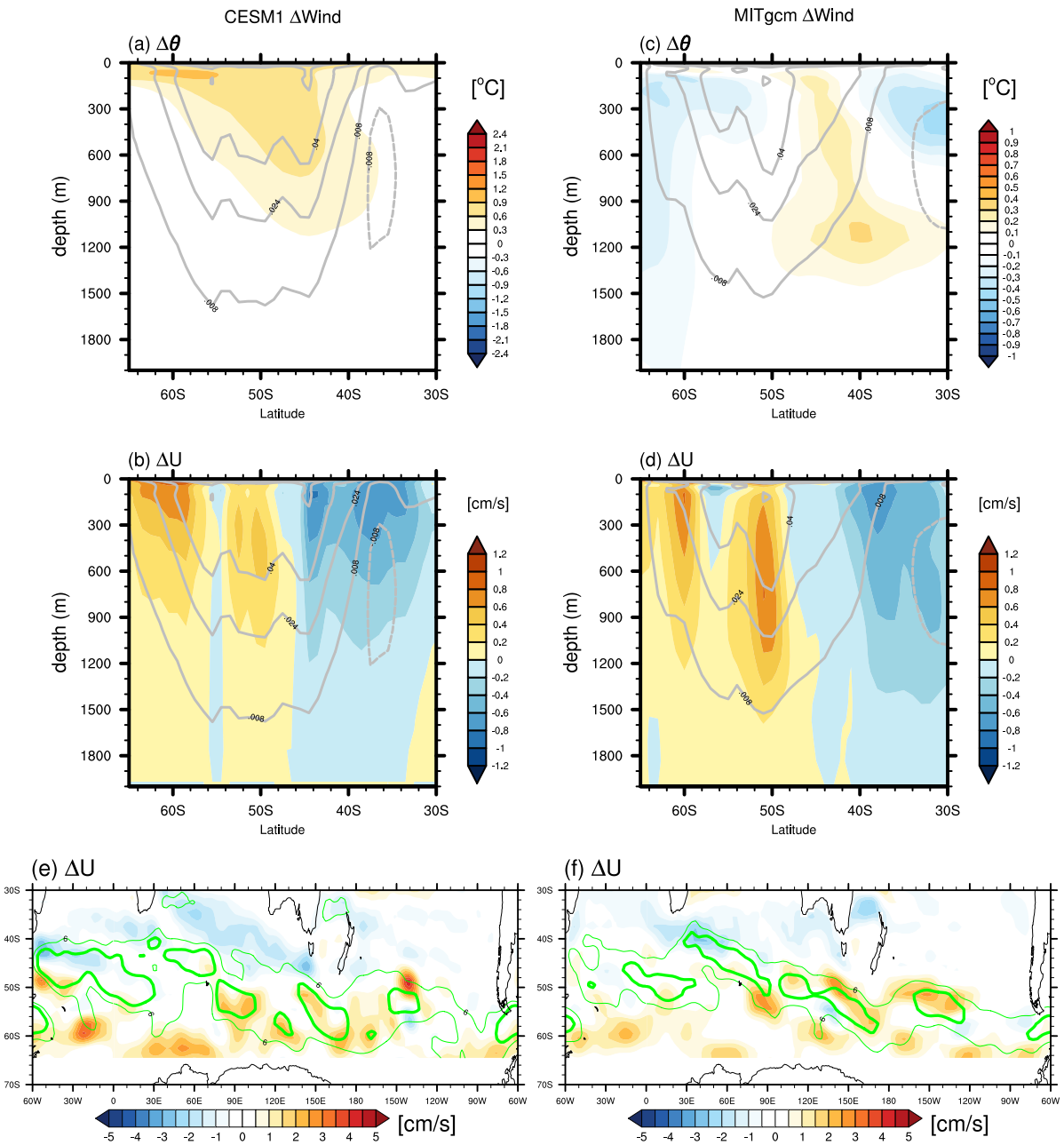

Extended Data Fig. 6 | Wind-change-induced temperature and zonal velocity changes. (**a**, **c**) Zonal mean potential temperature change and (**b**, **d**) U change induced by wind stress change (ΔWind) from CESM1_ΔWind (a, b) relative to CESM1_ΔBuoy and MITgcm_ΔWind (c, d) relative to MITgcm_CTL (Methods). Gray contours are the climatological zonal velocity U (in m/s) from the corresponding cases. Upper 100 m U change driven by wind stress change from (**e**) CESM1 and (**f**) MITgcm. Mean zonal velocities of 6 cm/s and 12 cm/s are shown as thin and thick green contours.

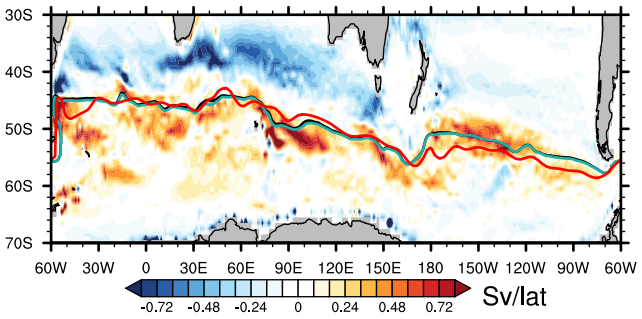

Extended Data Fig. 7 | Baroclinic transport change from CMIP6 ensemble mean and the position of mean 'SAF'. Upper 2,000 m baroclinic transport change (shadings) between 1998–2018 and 1940–1960 from CMIP6 ensemble mean. Black curve is the mean 'SAF' during 1940–1960 and cyan is the mean 'SAF' during 1998–2018. Red curve is the 1993–2019 mean 'SAF' based on the sea surface height from satellite observations.

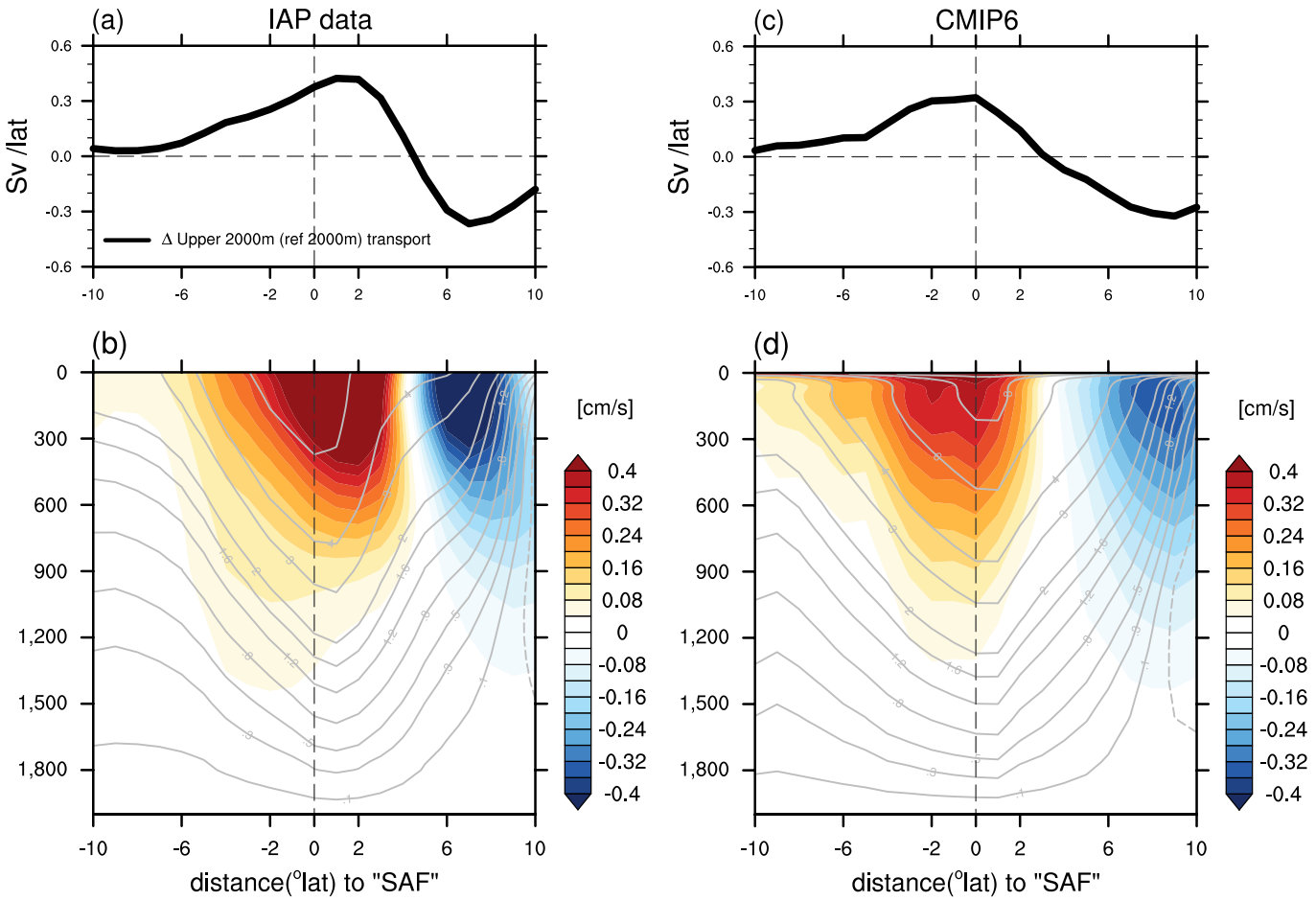

Extended Data Fig. 8 | Streamwise mean of upper 2,000 m baroclinic transport change and zonal velocity change. (**a**) upper 2,000 m baroclinic transport change and (**b**) zonal geostrophic velocity change between 1998–2018 and 1940–1960 from IAP data. The 'SAF' is defined as the observed 1993–2019 mean sea surface height passing through the Drake Passage at the point 67.5°W, 57.5°S. (**c**)-(**d**), same with (a)-(b), but the simulated velocity/transport change and the 'SAF' are based on CMIP6 ensemble mean. Gray curves in (b) and (d) are the streamwise mean climatological zonal velocity.

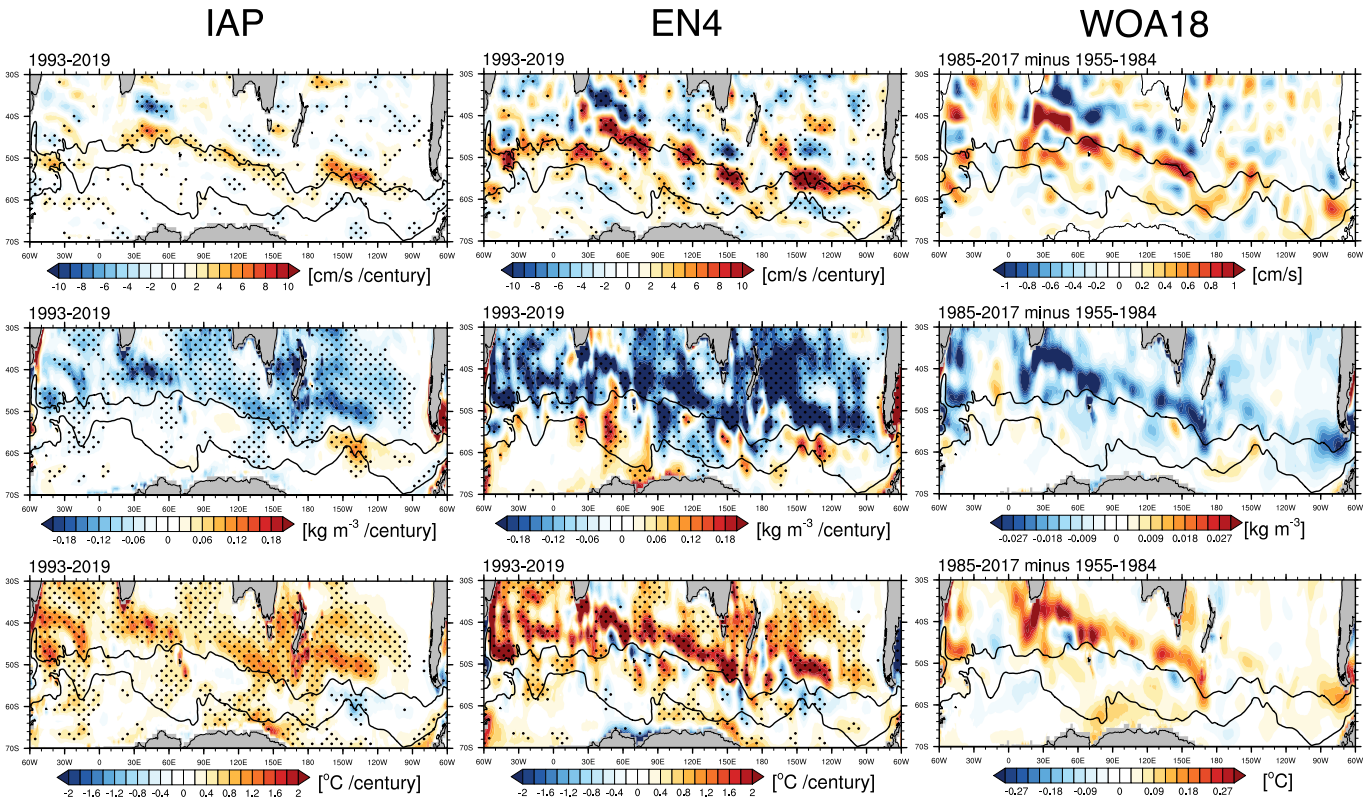

Extended Data Fig. 9 | Zonal velocity, potential density and potential temperature changes from observed datasets. Upper 100 m zonal geostrophic velocity, Ug, trend (1993–2019) from the IAP, EN4 and change from WOA18 (1985–2017 mean minus 1955–1984 mean) (top row). Corresponding trend/change of upper 2,000 m averaged potential density and potential temperature are shown in middle row and bottom row, respectively. Black contours indicate Subantarctic Front and Southern ACC Front. Stippling indicates regions exceeding 90% statistical significance computed from the two-tailed t-test.

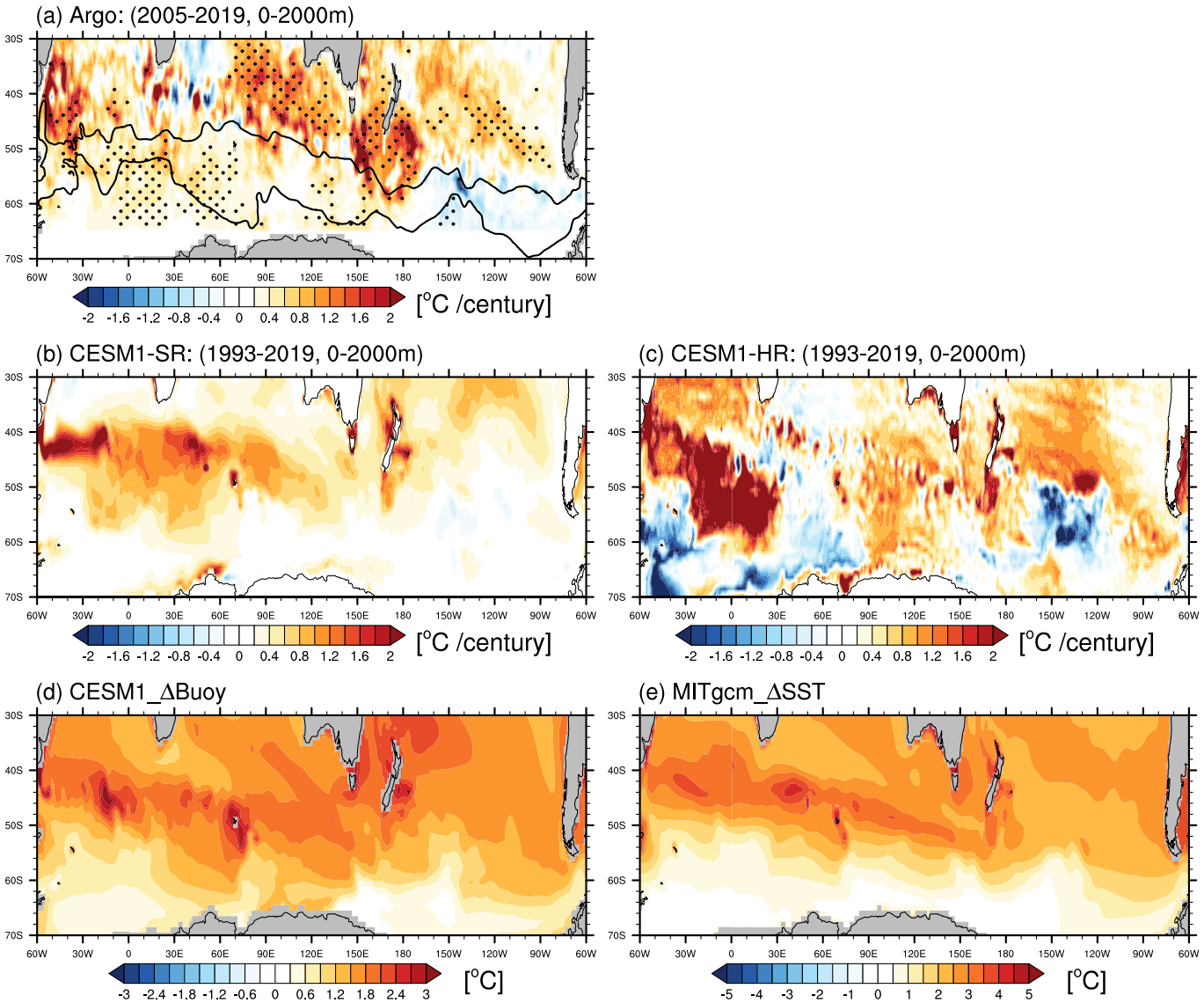

Extended Data Fig. 10 | Spatial patterns of temperature trend/change from Argo and model simulations. (**a**) Upper 2,000 m potential temperature trend from Argo observations (2005–2019). Black contours indicate the Subantarctic Front (SAF) and Southern ACC Front (SACCF). (**b**, **c**) Upper 2,000 m potential temperature trend from CESM1-SR (b) and CESM1-HR (c). (**d**, **e**) Upper 2,000 m potential temperature change from the CESM1_ΔBuoy experiment (d) and the MITgcm_ΔSST experiment (e) relative to the corresponding control runs. Stippling indicates regions exceeding 90% statistical significance computed from the two-tailed t test.